THE JOURNAL OF PHYSICAL CHEMISTRY C

pubs.acs.org/JPCC Article

# Unusual Li-ion Intercalation Activation with Progressive Capacity Increase in Orthosilicate Nanocomposite Cathode

Majid Rasool, Hsien-Chieh Chiu, Raynald Gauvin, De-Tong Jiang, Jigang Zhou, Dominic Ryan, Karim Zaghib, and George P. Demopoulos*

Cite This: J. Phys. Chem. C 2020, 124, 5966–5977 Read Online

ACCESS | Metrics & More | Article Recommendations | Supporting Information

**ABSTRACT:** Lithium iron silicate $Li_2FeSiO_4$ (LFS) has received significant attention as a Li-ion intercalation cathode material. However, it exhibits relatively poor Li-ion intercalation kinetics. In this work, mechanochemically annealed low-temperature orthorhombic ($\beta_{II}$, $Pmn2_1$) LFS@C nanocomposite is shown to exhibit unusual Li-ion intercalation activation during cycling. In particular, we present evidence of an impressive 2-fold capacity increase over an initial dozen cycles from 90 to 180 mAh $g^{-1}$. Interestingly a clear shift in Li-storage mechanism was triggered by the *in situ* activation of the orthosilicate structure from a solid solution to biphasic type. This unusual electrochemical behavior was further analyzed by a systematic study on surface chemistry and crystal structure. Surface chemistry evaluation revealed the formation of a thick LiF-rich layer during cycling, which enabled stable cycling. More strikingly, a progressive irreversible *in situ* phase transition during the initial dozen cycles was revealed, which activated ion transport by two orders of magnitude. Such an unreported electrochemically induced structural activation provides unexplored opportunities for unlocking the full potential of high capacity nanostructured orthosilicate and other types of Li-ion battery cathodes.

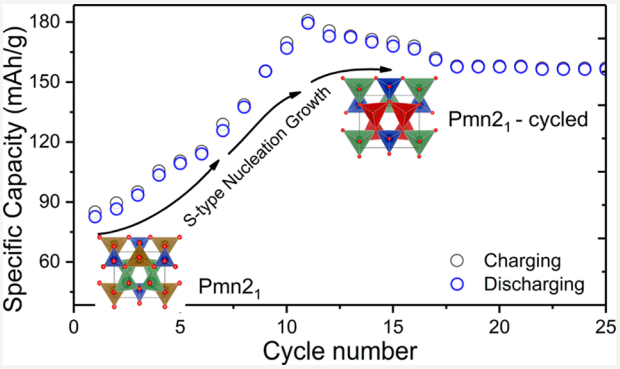




## 1. INTRODUCTION

Lithium ion batteries (LIBs) use intercalation compounds for both the anode and the cathode.[1,2] Since the initial commercialization of the $LiCoO_2$-graphite LIB in the early 90s,[3] we have seen, in recent years, significant progress in the development of improved intercalation materials with some of them reaching commercial levels, such as $LiNi_xMn_yCo_zO_2$, $LiFePO_4$ and $Li_4Ti_5O_{12}$ etc.[1,2,4,5] This was mainly achieved by evaluating and controlling their complex intercalation chemistry. Notably, all these materials have intrinsic limitations in terms of capacity, structural stability, and safety.[2,6]

In this context, polyanionic lithium iron orthosilicate ($Li_2FeSiO_4$) is of special interest due to its high theoretical capacity (331 mAh $g^{-1}$). This results from the $2e^-$ reaction mechanism which leads to double capacity in comparison to its commercial counterpart $LiFePO_4$.[7,8] The cathode material has also excellent safety against thermal runaway, low cost, and resource abundance for large-scale electric vehicle (EV) LIBs.[7,9−13] However, there are still major material chemistry challenges in transforming $Li_2FeSiO_4$ (LFS) into a high-performance cathode material. For example, it possesses different crystal phases due to very small differences in formation energies, which complicates the optimization of their properties for commercial cathode applications.[7,14−18] Almost all the recent theoretical and experimental studies indicate a phase transition from monoclinic $P2_1/n$ to the thermodynamically stable inverse $Pmn2_1$ phase during charging/discharging.[19−21] This type of irreversible phase transitions are typically associated with capacity fade during cycling as they prevent the fully reversible insertion of Li ions into these intercalation electrodes.[22−24] Thus, the issues of structural stability and long-term cyclability of LIBs are raised.

Similarly in the case of LFS, like other intercalation cathodes, several studies report capacity fade during cycling.[25−29] However, contrary to typical capacity fade behavior, there are reports which show that LFS exhibits gradual capacity increase during electrochemical cycling, although the authors failed to capture the significance of this phenomenon or study it further. For example, Xu et al.,[30] Fan et al.,[31] and Zhao et al.[32] have reported gradual capacity increases that stabilized after several cycles which the authors merely attributed to the electrolyte taking time to completely wet/infiltrate the cathode material; no surface or structural

Received: December 24, 2019
Revised: February 13, 2020
Published: February 21, 2020




https://dx.doi.org/10.1021/acs.jpcc.9b11896
J. Phys. Chem. C 2020, 124, 5966–5977

characterization was undertaken and no further hypothesis was given. Such a phenomenon has been observed, nevertheless, in the case of Li-rich layered oxide cathode materials.[33−35] Thus, Ye et al.[36−38] reported this gradual capacity increase for Li-rich layered oxides to relate to the *in situ* electrochemical activation of the $Li_2MnO_3$ phase prompted by metal doping. No other systems have been reported to exhibit such intriguing behavior. Therefore, it is of great interest to understand the origin of such an electrochemically induced activation process as it may lead to the nanoengineering of high-energy density cathodes with improved charging/discharging performance as is potentially the case with LFS.

To this end, we have synthesized the low-temperature orthorhombic phase ($Pmn2_1$) of $Li_2FeSiO_4$ using hydrothermal synthesis at 200 °C for 6 h. Due to poor Li-ion intercalation storage and conductivity of the low-temperature $Pmn2_1$ LFS phase, we subjected it to high-energy mechanochemical milling in the presence of carbon black at room temperature to render it as a LFS@C nanocomposite. As we have reported elsewhere, this mechanochemical treatment under controlled (time and rpm) conditions leads to crystal structure annealing in addition to nanosizing.[39] During the follow up electrochemical cycling of this material, we discovered that such a LFS@C nanocomposite exhibits electrochemical-induced structural activation leading to the doubling of its reversible capacity from 90 to ∼180 mAh $g^{-1}$. Interestingly, this impressive increase in charge capacity was associated with a simultaneous transition from the solid solution to a two-phase Li-ion storage mechanism clearly indicating an *in-operando* structural transformation unlike previous studies, which attributed such a capacity increase to mere electrolyte penetration. To further probe this behavior, we conducted an *ex situ* post-mortem analysis of the electrode surface chemistry using SEM, TEM, EDS, and XPS techniques revealing the formation of a lithium fluoride (LiF) layer at the solid electrolyte interphase (SEI). Bulk characterization performed by XRD, XANES, and EELS revealed progressive phase transition toward the inverse $Pmn2_1$ phase. This newly described cycling-induced electrochemical activation phenomenon of the mechanochemically prepared LFS@C nanocomposite opens a new avenue for developing high energy density nanosilicate cathodes for LIB applications.

## 2. EXPERIMENTAL SECTION

**2.1. Material Synthesis.** $Li_2FeSiO_4$ (LFS) was synthesized using a hydrothermal method adapted from Sirisopanaporn et al.[12] In a typical experiment, 200 mL of precursor solution was prepared using 0.01 mol of fumed silica ($SiO_2$), 0.01 mol of iron chloride ($FeCl_2{\cdot}4H_2O$), and 0.04 mol of lithium hydroxide monohydrate ($LiOH{\cdot}H_2O$). First, 0.04 mol of $LiOH{\cdot}H_2O$ was dissolved in deoxygenated water with stirring until a clear solution was obtained. Next, 0.01 mol of $SiO_2$ was added to the solution while the volume of the mixture was kept constant at 160 mL. This was followed by an ultrasonication step at 37 Hz for 1.5 h to achieve a clear mixture. The mixture was then transferred to a nitrogen-filled glovebox along with 0.01 mol of $FeCl_2{\cdot}4H_2O$. Then 0.01 mol of $FeCl_2{\cdot}4H_2O$ was dissolved in 40 mL of deoxygenated water (stored inside glovebox), and the mixture was stirred for 5 min. The ferrous chloride and Li/Si solutions were then mixed slowly using a peristaltic pump. Finally, the mixed solution was poured into a stainless-steel autoclave (450 mL capacity from PARR), equipped with a Teflon liner and closed inside the glovebox. The temperature was raised to 200 °C, and the mixture was stirred for 6 h at 300 rpm under an argon gas atmosphere. After being autoclaved, the cool-down precipitates were recovered by a centrifuge separator and washed with a saturated LiOH solution inside a $N_2$-filled glovebox. The product was further washed with acetone and dried under a vacuum for 12 h at 100 °C.

**2.2. High-Energy Milling.** To reduce the particle size of the ortho-LFS ($Pmn2_1$) powder, a planetary micro mill PULVERISETTE 7 premium line (Fritsch) was used. Solvent-assisted high-energy milling was employed to grind 0.8 g of ortho-LFS in 15 mL of isopropanol with grinding media (1 mm balls) of 50 g of zirconium oxide ($ZrO_2$) in each $ZrO_2$ milling jar (80 mL capacity). To increase the electronic conductivity of LFS, 10% carbon black (*vis-à-vis* the amount of LFS) was also added by keeping the same weight ratio. Milling cylinders were filled with LFS powder, solvent, and carbon black along with grinding media and sealed inside a glovebox under a $N_2$ atmosphere. All preparation steps were carried out inside the $N_2$-filled glovebox to avoid the oxidation of LFS. The sealed cylinders were transferred to a milling machine and typically milled for 5 cycles at 250 rpm, where each cycle lasted for 1 h as per the protocol established in our previous work.[39] The break between each cycle was 30 min. After the milling process, cylinders were then transferred back to the glovebox to use a centrifuge separator, and the samples were dried under a vacuum at 80 °C overnight.

**2.3. Material Characterization.** Microstructure analysis and electron diffraction techniques were performed with a Hitachi SU−8000 cold-field emission scanning electron microscope (SEM) and a Philips CM200 transmission electron microscope (TEM) at 200 kV, respectively. Electron energy loss spectroscopy (EELS) was performed with a Jeol JEM-2100F with a field effect gun operating at an acceleration voltage of 200 kV. For TEM/EELS samples preparation, active material electrodes (LFS@C nanocomposite) were carefully cleaned with DMC and dried (3−4 h) inside the glovebox. Subsequently, active material was scrapped from the aluminum current collector and transferred to a carbon grid. All samples were sealed inside the glovebox and degassed again for 30 min at the TEM/EELS workstation prior to data collection. A Micromeritics TriStar 3000 apparatus was used for $N_2$ adsorption/desorption in order to determine the Brunaer-Emmett-Teller (BET) surface area. Advanced synchrotron X-ray characterization was conducted at Canadian Light Source (CLS). The samples for powder X-ray diffraction (PXRD) analysis were loaded in 0.5 mm inner diameter Kapton capillaries which were sealed at both ends with a Loctite adhesive. Diffraction signals were collected using the Canadian Macromolecular Crystallography Facility beamline (CMCF-BM or 08B1-1) at CLS. 08B1-1 is a bending magnet beamline with a Si (111) double crystal monochromator. Two-dimensional (2D) data was obtained using a Rayonix MX300HE detector with an active area of 300 mm × 300 mm. The patterns were collected at an energy of 18 keV ($\lambda$ = 0.7523 Å) and a capillary−detector distance of 250 mm. The sample−detector distance, detector centering, and tilt were calibrated using a lanthanum hexaboride ($LaB_6$) standard reference material from the National Institute for Standards and Technology (NIST SRM 660a $LaB_6$), and the calibration parameters were applied to all patterns. After calibration, the 2D patterns were integrated to obtain standard 1D powder diffraction patterns. A pattern from an empty Kapton capillary was subtracted from the sample data during integration.


https://dx.doi.org/10.1021/acs.jpcc.9b11896
J. Phys. Chem. C 2020, 124, 5966−5977

TOPAS (Version 4.2, Bruker AXS, Karlsruhe, Germany) was employed for Rietveld refinement. X-ray absorption near edge structure (XANES) was performed at the Fe K-edge at 17 keV photon energy; energy calibration was performed by determining the first inflection point of the standard Fe and Yt XANES, for the respective energies. XANES samples were prepared by cleaning the active material electrodes with DMC and dried inside the glovebox for 3−4 h. Active material was scrapped and pasted onto the Kapton film and sealed inside the glovebox for data collection at CLS. X-ray photoelectron spectroscopy (K-Alpha XPS, Thermal Fisher Scientific Inc.) was performed for surface characterization. Raman spectroscopy (Bruker Senterra dispersive Raman microscope) and $^{57}$Fe Mössbauer spectroscopy were performed for bulk characterization.

**2.4. Electrochemical Tests.** A typical electrode was prepared as follows: a paste was prepared by mixing the high-energy milled active material LFS@C nanocomposite, carbon black, and binder polyvinylidene fluoride (PVDF) at a ratio 8:1:1 in *N*-methyl-2-pyrrolidone (NMP) solvent. All components were mixed thoroughly with manual grinding for about 30 min. The homogeneous paste was then cast onto ethanol-washed aluminum foil and dried for 2 h at 50 °C. After drying, the electrode sheet was transferred to a vacuum oven and kept overnight at 80 °C to remove any traces of solvent. After being dried, the electrode sheet was punched out into 1 cm diameter circles for half-cell assembly. Each final electrode contained approximately 2.1 mg cm$^{-2}$ of active material. A typical cell consisted of the above fabricated LFS-C-PVDF electrode as the cathode, lithium metal as the anode, and standard battery grade electrolyte comprising 1 M $LiPF_6$ dissolved in mixed EC/DMC (1:1 by volume) solvent, purchased from BASF and directly used after opening inside the glovebox. A polypropylene-polyethylene-polypropylene (PP/PE/PP) film (Celgard 2300) was used as a separator. The cells were stored in the glovebox for 24 h prior to electrochemical testing to allow for the complete wetting of electrodes by electrolyte. Galvanostatic charge−discharge cycling tests were performed at RT with the cycler from Arbin (BT2000) or the battery analyzer (model # BST8MA) from MTI Corporation, in the voltage range from 1.5 to 4.5 V vs $Li^+/Li$. Electrochemical impedance spectroscopy (EIS) and cyclic voltammetry (CV) were performed using a Bio-Logic VSP potentiostat and EC-Lab software for data analysis.

## 3. RESULTS AND DISCUSSION

**3.1. Mechanochemically Annealed LFS Nanocomposite.** The XRD pattern of $Li_2FeSiO_4$ (LFS), prepared by hydrothermal synthesis, can be found in the Supporting Information (SI) Figure S1. All peaks were correctly assigned, with the aid of TOPAS software, to Bragg positions of low-temperature orthorhombic phase ($\beta_{II}$, $Pmn2_1$) consistent with the results presented elsewhere.[40] Therefore, the as-prepared LFS by hydrothermal synthesis was phase pure (except minor iron oxide impurities estimated at ∼5%; refer to Figure S1 in the SI), which is certainly advantageous over high-temperature phases of LFS suffering from significant monoclinic and orthorhombic phase coexistence.[7,21] The SEM images in Figure S2 show that the hydrothermally synthesized secondary aggregated particles of as-prepared LFS have an average size of ∼1 $\mu$m. Notably, it is known that LFS suffers from low intrinsic conductivity properties (electronic and ionic) which hamper the lithium ion extraction and insertion processes. The $Li^+$ ion diffusion coefficient is very low, ranging between $10^{-12}$ and $10^{-20}$ cm$^2$ s$^{-1}$ at room temperature, which is obviously lower than that for the low conducting $LiFePO_4$ (∼$10^{-7}$ cm$^2$ s$^{-1}$).[41−43] It is well accepted that a nanoscale particle size provides short $Li^+$ ion diffusion path, which facilitates the Li intercalation kinetics in LFS electrode. As suggested by previous simulation and experimental studies, nanosizing, on one hand, and carbon coating, on the other, are good means to promote Li-ion diffusion and electronic conductivity, respectively.[14,44−47] However, the standard carbon coating process involves heating the active material with a carbon source like lactose at a temperature near 700 °C.[48] Since that temperature is likely to induce phase transition of the as-prepared low-temperature orthorhombic LFS ($Pmn2_1$) phase to the monoclinic ($P2_1/n$) phase,[19,21] the LFS particles were instead subjected to high-energy milling in the presence of carbon black under ambient conditions, building on our recent carbon-free mechanochemical-induced annealing work.[39] To this end, a pristine LFS sample was milled together with carbon black for 5 h at 250 rpm according to protocol established previously.[39] The resulting powder of the LFS@C nanocomposite was analyzed using XRD as shown in Figure 1a. All peaks can still be correctly assigned to the Bragg

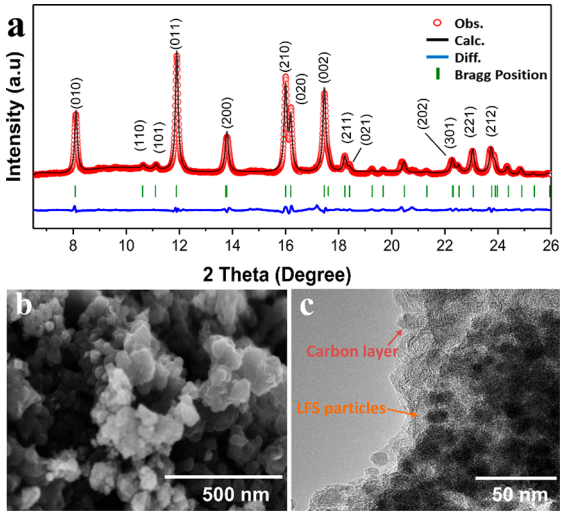


**Figure 1.** Synchrotron-based XRD pattern of LFS@C nanocomposite sample obtained after hydrothermal synthesis and mechanochemical annealing (synchrotron source, $\lambda$ = 0.7523 Å) and refined with $Pmn2_1$ space group ($R_{wp}$ = 4.20, $R_p$ = 3.43, and GOF = 2.38) using TOPAS software. Lattice parameter values obtained from fitting are $a$ = 6.29231 (Å), $b$ = 5.35212 (Å), and $c$ = 4.96224 (Å). (b) SEM and (c) TEM morphology of LFS@C nanocomposite showing nanoparticles covered with thin carbon layer as indicated with arrows.

position of low temperature orthorhombic phase ($\beta_{II}$, $Pmn2_1$) after mechanochemical annealing. It should be added also that according to the in-depth analysis presented in our recent work,[39] this type of mechanochemical annealing leads to the reduction of antisite defects and the simultaneous development of preferred crystal orientation. The LFS@C nanocomposite possessed a high BET surface area of 64.3 m$^2$ g$^{-1}$, extracted from $N_2$ adsorption−desorption isotherm plots shown in Figure S3. Further, SEM and TEM images are shown in Figure 1b,c. The SEM image shows the high-energy milled LFS particles with a reduced size of about 50 nm. This was further examined with TEM imaging as shown in Figure 1c, where a


https://dx.doi.org/10.1021/acs.jpcc.9b11896
J. Phys. Chem. C 2020, 124, 5966−5977

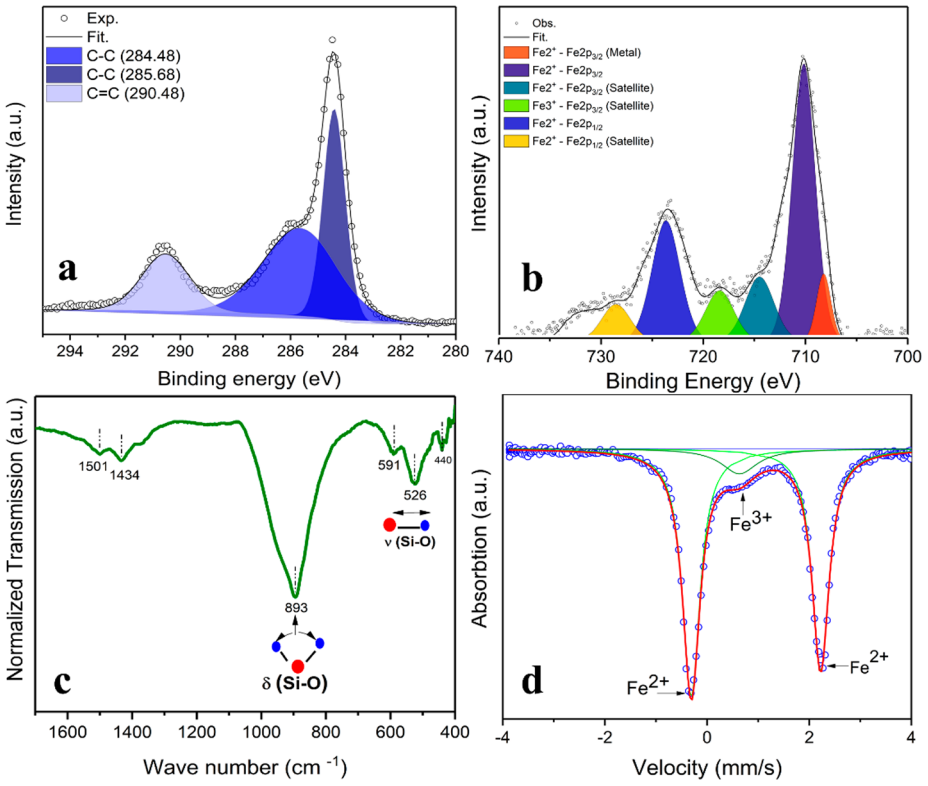


**Figure 2.** Characterization of carbon and iron species ($Fe^{2+}$ and $Fe^{3+}$) on the surface and in the bulk of LFS@C nanocomposite using XPS, FTIR, and Mössbauer spectroscopy, respectively. (a) XPS spectra of carbon, (b) XPS spectra of iron species ($Fe^{2+}$ and $Fe^{3+}$) on the surface, (c) FTIR spectra, and (d) Mössbauer spectra.

clearly distinguishable carbon layer is observed to envelop LFS nanoparticles in the carbon matrix; see also HRTEM in Figure S4. To further characterize the carbon layer in the LFS@C nanocomposite material, XPS, FTIR and Raman were performed. In Figure 2a, XPS spectra confirm the carbon layer on the surface of the LFS@C sample. In Figure S5, the Raman peaks at 1332 and 1595 $cm^{-1}$, typically corresponding to the D and G bands of graphite, provide further evidence on the existence of graphitized carbon.[49] Similarly, the FTIR spectra shown in Figure 2c indicate the presence of carbon bonds at 1501 and 1434 $cm^{-1}$, respectively, along with $SiO_4$ stretching and bending as indicated by the illustration in Figure 2c. Moreover, we checked the LFS@C nanocomposite for an Fe signal using XPS and Mössbauer spectra as shown in Figure 2b,d. In Figure 2b, the peak appearing at $2P_{3/2}$ with binding energy of 710.70 eV corresponds according to the fitting made with Advantage software to ferrous signal and a small ferric satellite signal. The minor presence of ferric was further confirmed by Mössbauer spectroscopy according to results in Figure 2d. The two peaks at ∼ −0.2 and ∼2.2 mm/s correspond to $Fe^{2+}$ contribution from the LFS sample. The minor peak appearing at ∼0.6 mm/s arises from $Fe^{3+}$ contribution apparently reflecting some superficial ferric iron formation from air exposure during handling. This was determined to be ∼8% similar to our previous work[50] and lower than that of other works reporting anywhere between 10% and 30% ferric iron.[7,51] The predominance of $Fe^{2+}$ in the mechanochemically annealed orthorhombic phase ($Pmn2_1$) LFS nanocrystals prior to cycling was also confirmed by EELS and XANES as per additional data presented later in Figure 8.

**3.2. Unusual Li-Ion Intercalation Activation.** Figure 3 shows different electrochemical measurements of LFS@C nanocomposite material. In Figure 3a,c, galvanostatic charging and discharging curves at a very low C-rate (C/50) and room temperature, almost near equilibrium, are shown separately for clarity for the first 11 cycles. Cycle number vs specific capacity (mAh $g^{-1}$) including Coulombic efficiency up to 50 cycles are shown in Figure 3e. As shown in Figure 3a,c (only some cycles are plotted for clarity), during the initial cycle, LFS@C delivers charge/discharge capacity of about 90 mAh $g^{-1}$. It must be noted here that the first discharge capacity of the pristine $Pmn2_1$ LFS is only about 30 mAh $g^{-1}$, which fades significantly upon cycling.[39] Such a low attained capacity is due to the structural "inactivity" of low T ortho-LFS that is overcome after mechanochemical annealing that has been shown to enhance ion transport via defect elimination.[39] But what is really interesting is that the mechanochemically prepared LFS@C nanocomposite after the first cycle not only did not exhibit capacity fade but showed instead an unusual electrochemically induced capacity increase response. Interestingly, the discharge capacity started to increase after each cycle, namely, from 90 to 180 mAh $g^{-1}$, i.e., a 2-fold increase from the 1st to the 11th cycles. The slight over one Li (180 vs 166 mAh $g^{-1}$) excess capacity may be attributed to the redox activity by lattice oxygen as reported previously by Masese et al.[52] as well as our group based on O K-edge XANES analysis[21] and DFT calculations[15] and less likely, due to relatively low potential (4.5 V), to the tetravalent iron.[53]

Another notable observation is that after the 5th cycle, there is not only a significant capacity increase but also a change in its electrochemical charge storage behavior from solid solution to two-phase mechanism[54] as indicated by a shift from slanted to plateau-like curves (marked by dashed lines in Figure 3c). This intriguing electrochemical behavior is further elucidated


https://dx.doi.org/10.1021/acs.jpcc.9b11896
J. Phys. Chem. C 2020, 124, 5966−5977

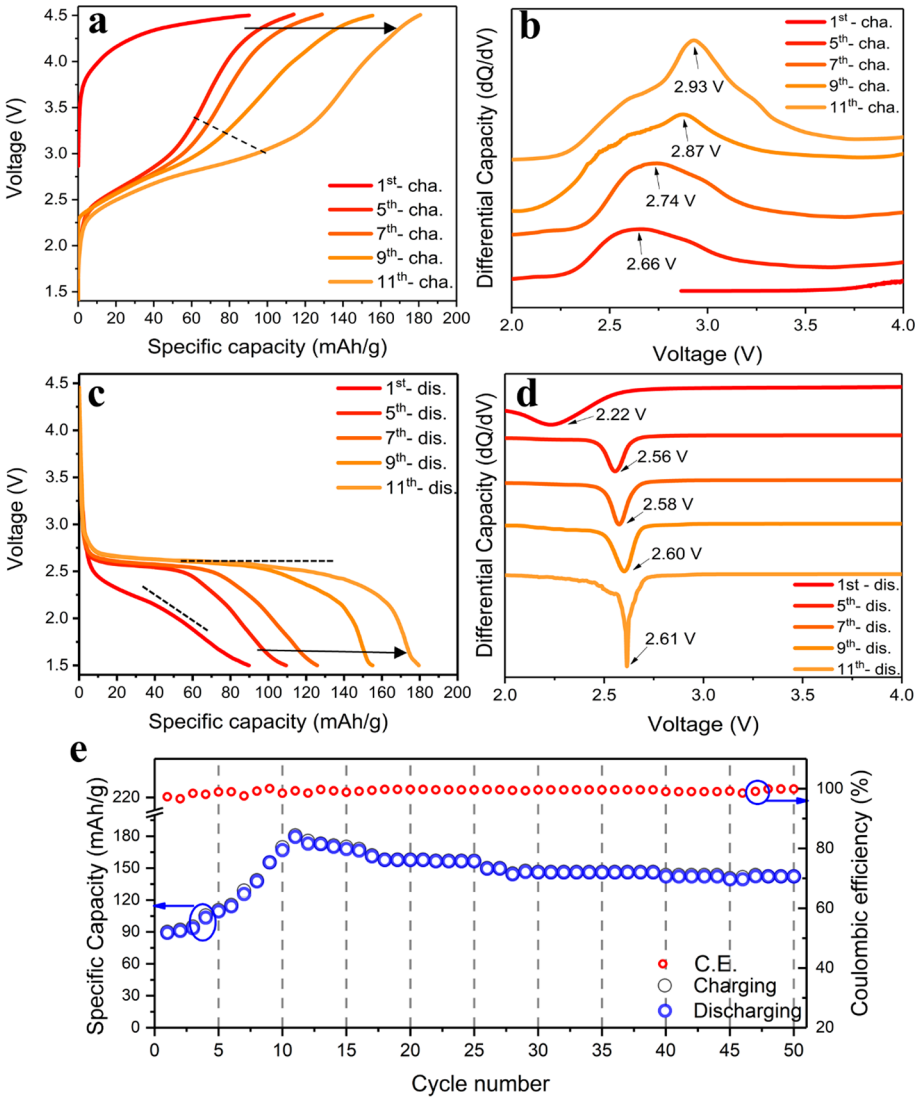


**Figure 3.** Electrochemical response of LFS@C nanocomposite samples. (a) Galvanostatic charging cycles at C/50 at room temperature and (b) their respective differential capacity curves (dQ/dV) along with cycle numbers. (c) Galvanostatic discharging cycles and (d) their respective differential capacity curves. (e) Cycle number vs specific capacity of LFS@C nanocomposite cycled at C/50 and room temperature (indicated in blue open circles) along with Coulombic efficiency as indicated in red using open circles.

by the generation of differential capacity plots from charge/discharge curves as shown in Figure 3b,d. Thus, as the capacity increased, both charge and discharge voltages increased from 2.66 to 2.93 V and 2.56 to 2.61 V, respectively, which reflects a complex phase evolution in silicates as noted in a previous study[21] (see 3.4 *In Situ* Crystal Phase Transition for a detailed discussion). At the same time, the intensity of the peaks became sharper and bigger in size, e.g., for charging profiles, the area under the peak for the 5th cycle increased from 0.12795 to 0.66618 after the 11th cycle. Similarly for discharging profiles, there is an increase in area under peak from the 1st cycle (0.0828) to the 11th cycle (0.1262). This clearly indicated that the lithium-ion intercalation storage had significantly improved after the cycling-induced electrochemical activation, which was also evident from the stabilized Coulombic efficiency (see Figure 3e) when compared to the initial cycles. Following this electrochemical activation, the capacity was self-adjusted (due to apparent structure relaxation) at around 140 mAh $g^{-1}$ after the 40th cycle as shown in Figure 3e and SI Figure S6. Interestingly, both Xu et al.[30] and Zhao et al.[32] separately observed this gradual capacity increase and subsequent stabilization; however, they did not observe any significant change in the Li-storage mechanism possibly due to cycling at a relatively high C-rate (0.2C and 1C, respectively). Meanwhile, Fan et al.,[31] did observe a significant change in the Li-storage mechanism after the 20th cycle along with a gradual capacity increase. However, all these authors did not highlight in any way the significance of this behavior, merely attributing it to the electrolyte taking time to completely wet/infiltrate the cathode material, nor did they perform any *ex situ* surface or crystal structural change characterization of the cycled cathode as reported subsequently in 3.3 *In Situ* LiF-Containing SEI Formation and 3.4 *In Situ* Crystal Phase Transition, where a clear phase transition is observed.

To evaluate and understand further this intriguing behavior, cyclic voltammetry (CV) was performed at a scanning rate of 0.05 mV/s in the voltage range from 1.5 to 4.5 V as shown in Figure 4a. From the CV profiles, the $Fe^{2+}$/ $Fe^{3+}$ redox couple for initial cycles can be seen located at about 2.49 V (along


https://dx.doi.org/10.1021/acs.jpcc.9b11896
J. Phys. Chem. C 2020, 124, 5966−5977

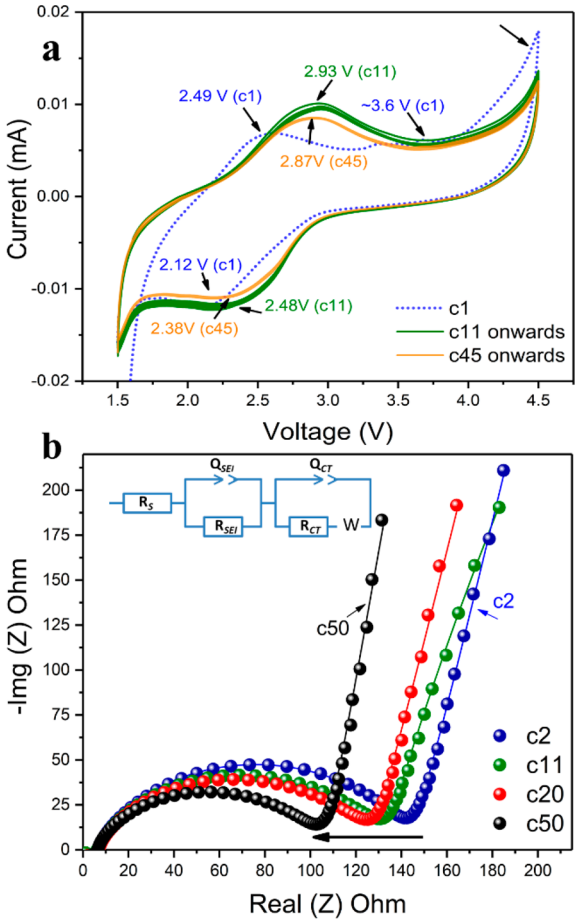


**Figure 4.** Electrochemical evaluation of LFS@C nanocomposite via (a) cyclic voltammetry at the scan rate of 0.05 mV/s and (b) impedance spectroscopy performed at room temperature (RT) between 1 MHz to 1 Hz.

with tiny peak at 3.6 V as indicated with arrows in Figure 4a) and 2.12 V versus $Li^+/Li$ for the charge and discharge, respectively. After the 10th cycle, we observed a significant shift of the redox couple peaks to 2.93/2.48 V, similar to voltage shifts obtained from differential capacity as shown in Figure 3b,d. In the meantime, the area under the peaks increased compared to those in the initial cycle. At the same time, the peaks increased in size clearly indicating that Lithium-ion intercalation storage had significantly improved, which confirmed our previous results obtained from the galvanostatic charging/discharging as shown in Figure 3. After the 45th cycle, the voltage reduced again and stabilized around the redox couple of 2.87/2.38 V. This redox potential shift of LFS@C during cycling is attributed to a change in the bonding environment (Fe−O) due to structural changes as in analogy and has been discussed for different LFS phases by Sirisopanaporn et al. and others.[16,55−57] This clearly aligns well with the presented galvanostatic cycling results suggesting that the observed gradual increase of capacity during cycling of LFS@C is associated with an underlying phase transition. Strikingly, the tail ends of the CV profiles decrease in size as well, indicating, possibly, the formation of a passivating SEI layer during cycling, as confirmed via SEM, TEM, and XPS in 3.3 *In Situ* LiF-Containing SEI Formation below.

Further, we collected electrochemical impedance spectroscopy (EIS) measurements as shown in Figure 4b along the equivalent circuit. The intercept at the Re(Z) axis represents the ohmic resistance ($R_s$) of the total resistances of electrolyte, separator, and electrical contacts. The $R_s$ value, as can be seen in Table S1, remains the same at 8.2 ± 0.1Ω from the 1st to the 50th cycle indicating that the electrodes that were well infiltrated with electrolyte were not responsible for the observed capacity increase, as suggested by previous works.[30−32] The semicircle at high frequency is related to the SEI layer, denoted as $R_{SEI}$. The semicircle at medium frequency range relates to the charge transfer resistance ($R_{ct}$). The inclined line is the Warburg impedance ($Z_W$), which is associated with $Li^+$ ion diffusion in the active particles.[58] The equivalent circuit is presented in the Figure 4b inset. It can be seen that as the LFS@C nanocomposite was cycled, the $R_{ct}$ decreased significantly in comparison to those in the initial cycles; please refer to Table S1 for fitting results. Meanwhile, $R_{SEI}$ increased significantly after the initial cycles due to the apparent growth of the passivating film as was further confirmed by SEM, TEM, and XPS results, discussed in detail in 3.3 *In Situ* LiF-Containing SEI Formation. Moreover, the EIS spectra of "pristine electrode" of LFS@C and after cycling are shown in Figure S7 and Table S2 (at a very low frequency of 0.5 mHz); from these, it can be clearly deduced that diffusion kinetics had considerably improved upon cycling. This electrochemical performance improvement is linked to the cycling-induced phase transition as elaborated in detail in 3.4 *In Situ* Crystal Phase Transition that leads to *in situ* activation of the intercalation process.

**3.3. *In Situ* LiF-Containing SEI Formation.** The intriguing behavior of the LFS@C nanocomposite prompted us to look further into what happened during the electrochemical cycling. As an initial guess, we debated whether this apparent phase transition during cycling was due to *in situ* surface alteration or bulk structure change. Therefore, initially, LFS@C was investigated using SEM and TEM. In Figure 4a, SEM morphology of pristine electrode is shown, where the LFS@C electrodes are dispersed in carbon black and PVDF. Interestingly, after the 5th cycle, the electrode morphology started to change, and it appeared to be covered by a thin layer (SEI); this continued as the material was cycled further. After 30 cycles, a very thick SEI layer was formed as shown in Figure 5d. When the electrodes were handled, some cracks were formed with a visible layer underneath, which again confirmed the thick SEI layer formation on the surface, as shown in SI Figure S8. This was further probed with TEM imaging technique as shown in Figure 5e−h. For the pristine electrode sample, we can see that the LFS@C nanoparticles are dispersed in the carbon and the binder, as distinguished by Z-contrast. However, after cycling for 30 cycles, the Z-contrast increased significantly. Further evidence can be seen in SI Figure S9, where the EDS maps, which were collected along with TEM, are shown. For the pristine electrode, the elements O, C, Fe, and Si were present. However, after the 30th cycle, a new peak corresponding to Fluorine (F) was observed, which indicated the possible formation of a LiF-containing SEI layer.[59] This was also confirmed by the collection of the *f*-ratio maps as shown in Figure 5i and Figure S10, where the F signal was seen to have significantly suppressed the signals of the other elements after cycling (30th cycle). To further confirm this finding, XPS measurements were also made, as shown in Figure 6, comparing the pristine electrode to the cycled LFS@C electrode. Only the fluorine signal is plotted here for discussion. The F signal coming from the binder (PVDF in our


https://dx.doi.org/10.1021/acs.jpcc.9b11896
J. Phys. Chem. C 2020, 124, 5966−5977

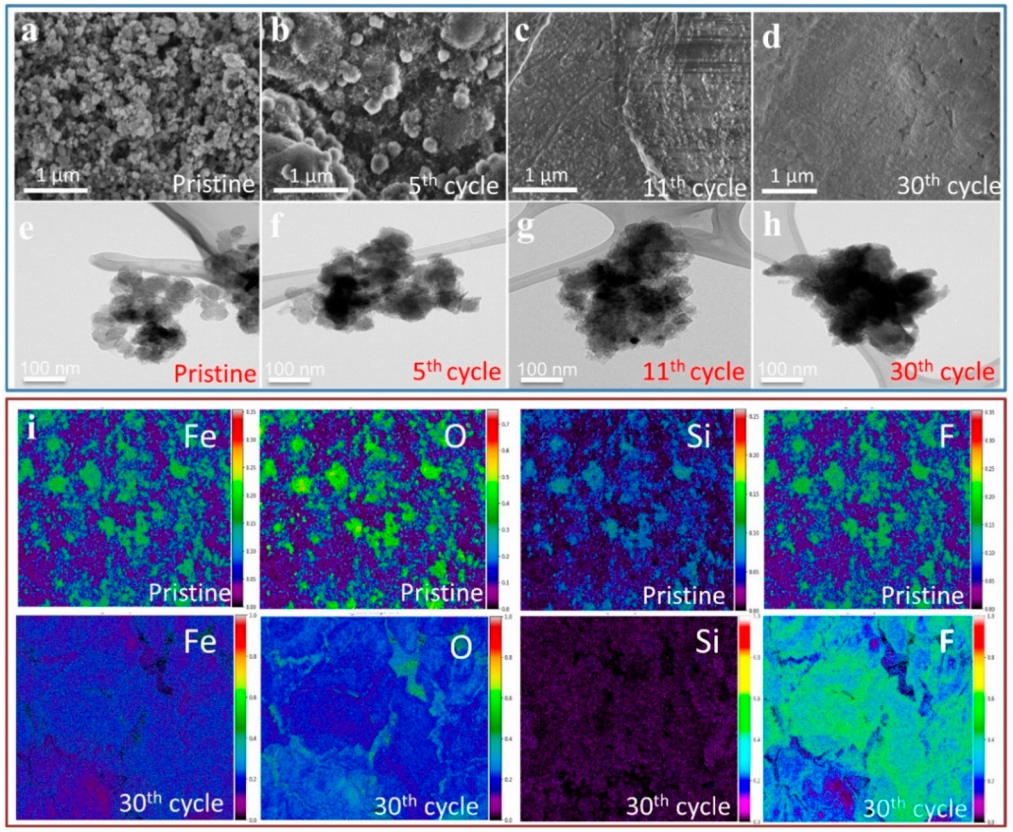


**Figure 5.** Post-mortem analysis of LFS@C nanocomposite samples by comparing the morphology of pristine electrode with cycled electrodes. (a) SEM morphology of pristine electrode of LFS@C nanocomposite sample and after (b) 5th, (c) 11th, and (d) 30th cycles, collected at fully discharged state, respectively. Similarly, (e) TEM morphology of pristine electrode sample LFS@C nanocomposite sample and after (f) 5th, (g) 11th, and (h) 30th cycles. (i) EDS maps were collected to probe the chemical changes induced on the surface after cycling. Here, *f*-ratio maps for fluoride, iron, oxygen, and silicon are shown for pristine electrode and after 30th discharge cycle, respectively. *f*-Ratio is defined as $f = \frac{I_A}{I_A + I_B}$ where $I_A$ and $I_B$ are the net characteristic X-ray intensities in one spectrum.[60]

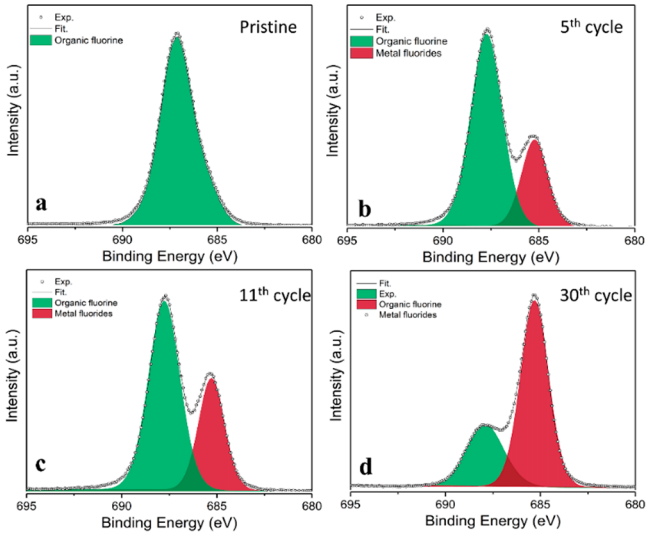


**Figure 6.** XPS conducted before and after cycling for identification of species on the surface. (a) Pristine LFS@C nanocomposite electrode before cycling and discharge-state electrodes after (b) 5th, (c) 11th, and (d) 30th cycles.

case) was obtained for the pristine electrode before cycling. After 5 cycles, a new peak started to emerge at 610 eV. This indicated the presence of a metal fluoride F signal, which confirmed the TEM results (see Figure 5) of SEI formation with LiF. After the 11th cycle, this peak increased further in size, which confirmed our previous results of SEM/TEM and EDS results. After the 30th cycle, the electrode surface showed a very strong signal from the metal fluoride F, which must have emerged from LiF as suggested before. The formation of such a LiF layer was previously reported to have taken place on LFS that was exposed to $LiPF_6$ electrolyte.[61−63] Similarly, in our case, LiF was formed on the interface of the exposed LFS@C nanocomposite cycled electrodes. Moreover, the formation of LiF during cycling was shown to act as a passive layer allowing the intercalation electrode to have long-term stability.[64] However, in our case, more in-depth analysis is required to understand the origin of the increased capacity that was observed during cycling.

**3.4. *In Situ* Crystal Phase Transition.** We further examined this phenomenon with XRD, EELS, and XANES spectroscopy techniques. We analyzed cells at the discharged state after the 5th, 11th, and 30th cycles to probe the crystal changes the LFS underwent during electrochemical galvanostatic cycling. These cycles were selected in particular based on the results reported in Figure 3a,c, as during those discharge cycles, the electrochemical response of LFS@C nanocomposite changed from sloped curves indicative of a solid solution to a plateau-like two-phase mechanism.

The investigation of the samples with synchrotron-based XRD is shown in Figure 7a. As can be seen from the pristine


https://dx.doi.org/10.1021/acs.jpcc.9b11896
J. Phys. Chem. C 2020, 124, 5966−5977

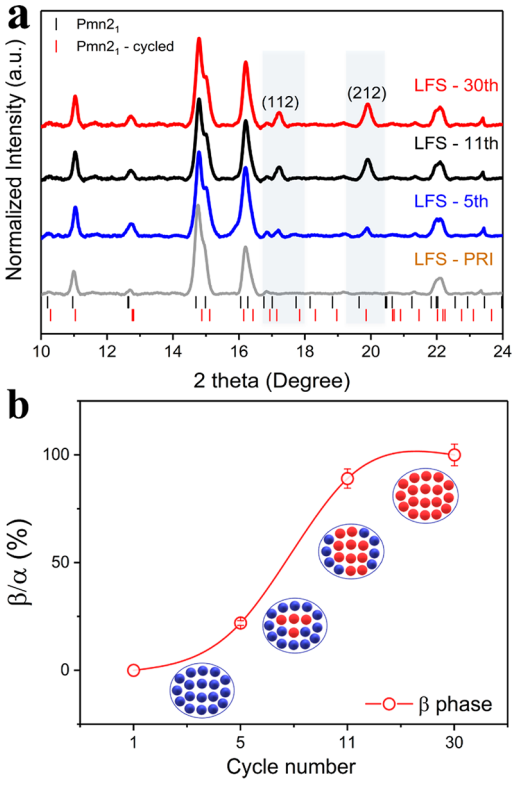


**Figure 7.** (a) Post mortem analysis of LFS@C nanocomposite electrodes using synchrotron-based XRD. Data was collected for pristine electrode and cycled electrodes (at fully discharged state) after 5th, 11th, and 30th discharge cycles. (b) New phase ($\beta$) percentage was calculated using XRD data and plotted vs number of cycles along with schematics of phase transition-activation.

LFS@C nanocomposite electrode, all the peaks correspond to the $Pmn2_1$ phase. However, after a few cycles, namely, at the 5th cycle, we can clearly distinguish the 5th cycle pattern from that of the pristine LFS@C nanocomposite electrode, as there are two new tiny peaks that emerge (marked with shaded bars) and are attributed to the (112) and (212) planes of an inverse $Pmn2_1$ phase (simulated patterns of both phases are shown in Figure S11). These two new peaks kept growing from the 5th to the 11th cycle. This indicated a clear *in situ* electrochemically induced irreversible phase transition corresponding to the unusual electrochemical response of LFS@C nanocomposite. After the 30th cycle, no apparent significant increase or growth of the two peaks was observed. These two new peaks can be assigned to a known phase of inverse $\beta_{II}$, $Pmn2_1$ (fitting results are shown in Figure S12). It is also possible that we have a new polymorph of LFS depending on the degree of cation mixing and amount of distortion in the structure upon cycling,[7,17] which would require additional in-depth crystal analysis. However, here, we would like to emphasize that the structural changes during galvanostatic cycling are clearly evident from the XRD results, revealing a new irreversible phase transition. In Figure 7b, the phase transition percentage of the $\beta$ (new) phase against the original mother matrix is calculated and its formation is described by a S-type nucleation-growth crystallization kinetic model,[23,65] namely, as lag phase, nucleation phase, and plateau phase. The electrochemical phenomena that occurred previously (see Figure 3 and Figure S6) can be explained with the aid of Figure 7b, where after the first cycles, no apparent crystal changes occurred (lag phase); however, after the 5th cycle, the $\beta$ phase started emerging (~25%) (nucleation stage) and thereafter entered the growth stage (~90% after the 11th cycle corresponding to almost 1 lithium extraction; see Figure 3 and Figure S6), eventually reaching the point of no-further transition after the 30th cycle, signaling the attainment of the stabilized discharge capacity range. These phase changes have important ramifications in terms of intercalation kinetics, as it is known that the $Pmn2_1$ phase has only 2D $Li^+$ ion diffusivity, whereas the inverse $Pmn2_1$ phase (cation mixing) obtained after cycling has 3D diffusivity pathways (crystal structure model illustrations are shown in Figure S13)[16,17] hence activating the electrochemical performance of the LFS@C nanocomposite material as shown in Figure 3.

We further probed the discharge cycled material using EELS and XANES spectroscopy. Figure 8a,b shows the EELS O-K edge and Fe-$L_{2,3}$ spectra of the pristine LFS@C nanocomposite electrode, 5th, 11th, and 30th cycle discharged cathode materials. Oxygen K-edge showed characteristic peaks at 538 eV for all selected discharge cells, while no significant changes occurred during cycling. Although the feature assignment of the O K-edge spectrum is not clear yet, we can be certain that the pre-edge at about 531 eV is directly related to the orbital hybridization of $FeO_4$ tetrahedra. According to our previous research, Lu et al.[21] reported that the monoclinic LFS exhibits similar pre-edge features attributed to the hybridization of oxygen and $Fe^{2+}$ with the ideal spin of 4. In other words, this feature can be used as an indication of the degree of Fe−O covalency. In the meantime, $Fe^{3+}$ with higher spin would lead to a new feature at lower energy because of its higher effective nuclear charge transfer.[21,66,67] For all selected discharge cycles, only subtle changes are evident. Thus, after the 11th cycle, a subtle pre-edge feature emerged that disappeared after the 30th cycle, which means the stable cycled LFS phase exhibited lower covalency. Other than this peak variation upon cycling, there was no new feature formed indicating that the crystal was completely relithiated at the discharged state of $Li_2FeSiO_4$. In Figure 8b, the Fe-$L_{2,3}$ spectra of the pristine after 5th, 11th, and 30th cycled materials are shown, according to which only $Fe^{2+}$ species are present. In this case, the peak observed at 710 eV corresponds to the $Fe^{2+}$ feature. There was no significant intensity and peak shift, indicating that no ferric was present at the discharge state. This confirms our previous results of O K-edge. Finally, we probed the pristine electrode and the electrode after 30th cycle with Fe K-edge XANES; the respective spectra are shown in Figure 8c. Here, in a comparison of the pristine sample (black line) with the cycle sample (red line), a slight shift in energy from pristine to the 30th cycle sample can be observed along with some transformation of the postedge features. These spectral features thus provide further evidence that LFS has undergone irreversible phase transition, clearly confirming the phenomena discussed earlier in Figure 7. Similarly, in SI Figure S14, where the pre-edge was plotted by extracting the background, we see that there was no significant change occurring after 30th cycle, indicating that LFS was fully lithiated and transformed into a new phase as mentioned previously. The observed change in peak symmetry is therefore attributed to the continuous evolution of structure during cycling. Figure 8d shows the Fe K-edge Fourier transform EXAFS spectra of pristine electrode and after 30 cycles. The first main peak (indicated with dashed vertical lines) corresponds to the Fe−O shell mode. Before and after cycling, there is a slight increase in the Fe−O bond


https://dx.doi.org/10.1021/acs.jpcc.9b11896
J. Phys. Chem. C 2020, 124, 5966−5977

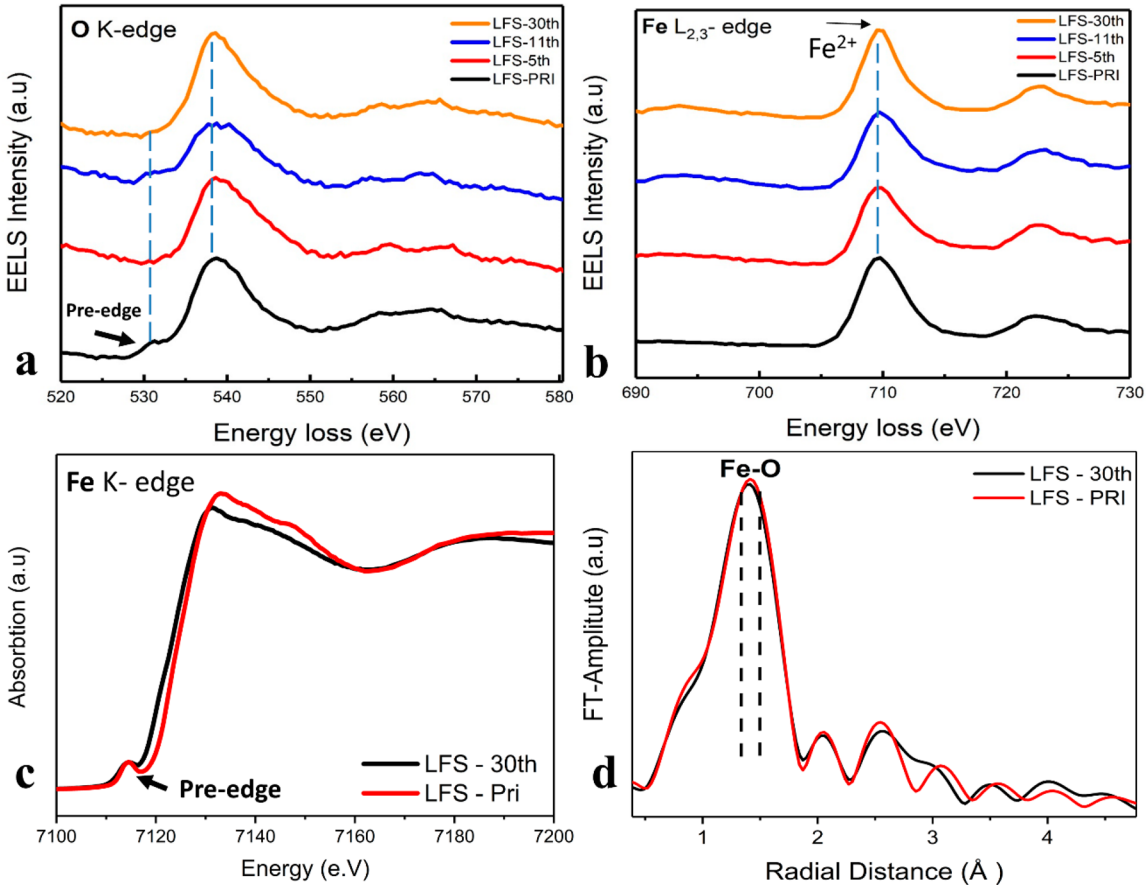


**Figure 8.** Electron energy loss spectroscopy (EELS) of (a) oxygen K-edge and (b) Fe $L_{2,3}$-edge for LFS@C nanocomposite electrodes before (pristine) and after charging/discharging for 5, 11, and 30 cycles. Electrodes were characterized at fully discharged state. (c) Similarly, the normalized Fe K-edge XANES spectra before (pristine) and after 30 cycles. (d) Fe K-edge Fourier transformed EXAFS spectra before (pristine) and after 30 cycles.

length, which is directly related to its different crystal phases, which in our case, is transitioning from normal $Pmn2_1$ to inverse $Pmn2_1$ phase.[7,39,55] This observation confirms our previous results of phase transformation.[55] These results shed new light on the complex intercalation chemistry of silicate cathodes paving the way toward attainment of their full capacity potential.

## 4. CONCLUSION

An understanding of the evolution of the complex phase transition mechanism and its control in $Li_2FeSiO_4$ plays a key role in unlocking its full capacity potential. Strikingly, in this study, mechanochemically annealed LFS@C nanocomposite manifested an unexpected *in situ* electrochemical activation behavior. The cycling at near equilibrium conditions (C/50) showed an impressive capacity increase during the initial dozen cycles. Notably, during cycling, its Li-storage mechanism transitioned as well from solid solution to biphasic type, which gave birth to progressive capacity increase. Unlike suggestions in previous studies, electrolyte infiltration is not the reason behind this impressive capacity increase. Upon surface chemistry characterization, the formation of a passivating LiF layer was revealed which contributes to long-term cyclability by preventing side reactions. In the meantime, a post-mortem analysis of the cathode after different numbers of cycles revealed LFS to undergo transformation to the inverse $Pmn2_1$ phase via a S-type nucleation-growth kinetic model in striking correspondence with the observed gradual increase of capacity and the biphasic storage mechanism. This type of largely, previously unnoticed electrochemically induced structural activation of the Li-ion storage process not only provides new insight into the dynamics of intercalation materials but also offers new means of optimizing the performance of high-density Li-ion battery electrodes.

## ■ ASSOCIATED CONTENT

### Supporting Information

The Supporting Information is available free of charge at https://pubs.acs.org/doi/10.1021/acs.jpcc.9b11896.

Characterizations of pristine LFS and LFS@C nanocomposite; *in situ* electrochemical phase transition evaluation of LFS@C nanocomposite via EIS; illustration of Li-ion diffusion in inverse $Pmn2_1$ crystal phase; *ex situ* post-mortem characterizations of LFS@C nanocomposite (PDF)

## ■ AUTHOR INFORMATION

### Corresponding Author

**George P. Demopoulos** − *Materials Engineering, McGill University, Montreal, QC H3A 0C5, Canada;* orcid.org/0000-0001-8112-5339; Phone: 514-398-2046; Email: george.demopoulos@mcgill.ca; Fax: 514-398-4492



https://dx.doi.org/10.1021/acs.jpcc.9b11896
J. Phys. Chem. C 2020, 124, 5966−5977

## Authors

**Majid Rasool** − *Materials Engineering, McGill University, Montreal, QC H3A 0C5, Canada;* orcid.org/0000-0001-8376-9146

**Hsien-Chieh Chiu** − *Materials Engineering, McGill University, Montreal, QC H3A 0C5, Canada*

**Raynald Gauvin** − *Materials Engineering, McGill University, Montreal, QC H3A 0C5, Canada*

**De-Tong Jiang** − *Department of Physics, University of Guelph, Guelph, ON N1G 2W1, Canada; Canadian Light Source, Saskatoon, SK S7N 2 V3, Canada*

**Jigang Zhou** − *Canadian Light Source, Saskatoon, SK S7N 2 V3, Canada;* orcid.org/0000-0001-6644-2862

**Dominic Ryan** − *Department of Physics, McGill University, Montreal, QC H3A 2T8, Canada*

**Karim Zaghib** − *Centre d'excellence-ETSE, Hydro-Québec, Varennes, QC, Canada;* orcid.org/0000-0002-4201-7746

Complete contact information is available at: https://pubs.acs.org/10.1021/acs.jpcc.9b11896


## Notes

The authors declare no competing financial interest.

## ■ ACKNOWLEDGMENTS

This work was supported through a Hydro-Québec/Natural Sciences & Engineering Research Council of Canada (NSERC) Collaborative R&D research grant (463484-2014). Synchrotron radiation measurements were performed at the CLS (Canadian Light Source).

## ■ REFERENCES


(1) Nitta, N.; Wu, F.; Lee, J. T.; Yushin, G. Li-Ion Battery Materials: Present and Future. *Mater. Today* **2015**, *18* (5), 252−264.

(2) Goodenough, J. B.; Park, K.-S. The Li-Ion Rechargeable Battery: A Perspective. *J. Am. Chem. Soc.* **2013**, *135* (4), 1167−1176.

(3) Van Schalkwijk, W.; Scrosati, B. In *Advances in Lithium-Ion Batteries*; Springer: Boston, 2002; pp 1−5.

(4) Etacheri, V.; Marom, R.; Elazari, R.; Salitra, G.; Aurbach, D. Challenges in the Development of Advanced Li-Ion Batteries: A Review. *Energy Environ. Sci.* **2011**, *4* (9), 3243−3262.

(5) Scrosati, B.; Hassoun, J.; Sun, Y.-K. Lithium-Ion Batteries. A Look into the Future. *Energy Environ. Sci.* **2011**, *4* (9), 3287−3295.

(6) Whittingham, M. S. Ultimate Limits to Intercalation Reactions for Lithium Batteries. *Chem. Rev.* **2014**, *114* (23), 11414−11443.

(7) Ni, J. F.; Jiang, Y.; Bi, X. X.; Li, L.; Lu, J. Lithium Iron Orthosilicate Cathode: Progress and Perspectives. *ACS Energy Lett.* **2017**, *2* (8), 1771−1781.

(8) Ferrari, S.; Capsoni, D.; Casino, S.; Destro, M.; Gerbaldi, C.; Bini, M. Electrochemistry of Orthosilicate-Based Lithium Battery Cathodes: A Perspective. *Phys. Chem. Chem. Phys.* **2014**, *16* (22), 10353−10366.

(9) Islam, M. S.; Dominko, R.; Masquelier, C.; Sirisopanaporn, C.; Armstrong, A. R.; Bruce, P. G. Silicate Cathodes for Lithium Batteries: Alternatives to Phosphates? *J. Mater. Chem.* **2011**, *21* (27), 9811−9818.

(10) Girish, H. N.; Shao, G. Q. Advances in High-Capacity $Li_2MSiO_4$ (M = Mn, Fe, Co, Ni,···) Cathode Materials for Lithium-Ion Batteries. *RSC Adv.* **2015**, *5* (119), 98666−98686.

(11) Tan, R.; Yang, J.; Zheng, J.; Wang, K.; Lin, L.; Ji, S.; Liu, J.; Pan, F. Fast Rechargeable All-Solid-State Lithium Ion Batteries with High Capacity Based on Nano-Sized $Li_2FeSiO_4$ Cathode by Tuning Temperature. *Nano Energy* **2015**, *16*, 112−121.

(12) Sirisopanaporn, C.; Dominko, R.; Masquelier, C.; Armstrong, A. R.; Mali, G.; Bruce, P. G. Polymorphism in $Li_2(Fe,Mn)SiO_4$: A Combined Diffraction and Nmr Study. *J. Mater. Chem.* **2011**, *21* (44), 17823−17831.

(13) Ellingsen, L. A.-W.; Hung, C. R.; Majeau-Bettez, G.; Singh, B.; Chen, Z.; Whittingham, M. S.; Strømman, A. H. Nanotechnology for Environmentally Sustainable Electromobility. *Nat. Nanotechnol.* **2016**, *11* (12), 1039−1051.

(14) Yang, J. L.; Zheng, J. X.; Kang, X. C.; Teng, G. F.; Hu, L.; Tan, R.; Wang, K.; Song, X. H.; Xu, M.; Mu, S. C.; Pan, F. Tuning Structural Stability and Lithium-Storage Properties by D-Orbital Hybridization Substitution in Full Tetrahedron $Li_2FeSiO_4$ Nanocrystal. *Nano Energy* **2016**, *20*, 117−125.

(15) Lu, X.; Chiu, H.-C.; Bevan, K. H.; Jiang, D.-T.; Zaghib, K.; Demopoulos, G. P. Density Functional Theory Insights into the Structural Stability and Li Diffusion Properties of Monoclinic and Orthorhombic $Li_2FeSiO_4$ Cathodes. *J. Power Sources* **2016**, *318*, 136−145.

(16) Saracibar, A.; Van der Ven, A.; Arroyo-de Dompablo, M. E. Crystal Structure, Energetics, and Electrochemistry of $Li_2FeSiO_4$ Polymorphs from First Principles Calculations. *Chem. Mater.* **2012**, *24* (3), 495−503.

(17) Lv, X.; Zhao, X.; Wu, S.; Nguyen, M. C.; Zhu, Z.; Lin, Z.; Wang, C.-Z.; Ho, K.-M. Fe−Si Networks and Charge/Discharge-Induced Phase Transitions in $Li_2FeSiO_4$ Cathode Materials. *Phys. Chem. Chem. Phys.* **2018**, *20* (21), 14557−14563.

(18) Vajeeston, P.; Fjellvag, H. First-Principles Study of Structural Stability, Dynamical and Mechanical Properties of $Li_2FeSiO_4$ Polymorphs. *RSC Adv.* **2017**, *7* (27), 16843−16853.

(19) Lu, X.; Wei, H.; Chiu, H.-C.; Gauvin, R.; Hovington, P.; Guerfi, A.; Zaghib, K.; Demopoulos, G. P. Rate-Dependent Phase Transitions in $Li_2FeSiO_4$ Cathode Nanocrystals. *Sci. Rep.* **2015**, *5*, 8599.

(20) Masese, T.; Orikasa, Y.; Tassel, C.; Kim, J.; Minato, T.; Arai, H.; Mori, T.; Yamamoto, K.; Kobayashi, Y.; Kageyama, H.; Ogumi, Z.; Uchimoto, Y. Relationship between Phase Transition Involving Cationic Exchange and Charge-Discharge Rate in $Li_2FeSiO_4$. *Chem. Mater.* **2014**, *26* (3), 1380−1384.

(21) Lu, X.; Chiu, H.-C.; Arthur, Z.; Zhou, J.; Wang, J.; Chen, N.; Jiang, D.-T.; Zaghib, K.; Demopoulos, G. P. Li-Ion Storage Dynamics in Metastable Nanostructured $Li_2FeSiO_4$ Cathode: Antisite-Induced Phase Transition and Lattice Oxygen Participation. *J. Power Sources* **2016**, *329*, 355−363.

(22) Vetter, J.; Novák, P.; Wagner, M. R.; Veit, C.; Möller, K.-C.; Besenhard, J.; Winter, M.; Wohlfahrt-Mehrens, M.; Vogler, C.; Hammouche, A. Ageing Mechanisms in Lithium-Ion Batteries. *J. Power Sources* **2005**, *147* (1−2), 269−281.

(23) Chiu, H. C.; Lu, X.; Zhou, J.; Gu, L.; Reid, J.; Gauvin, R.; Zaghib, K.; Demopoulos, G. P. Capacity Fade Mechanism of $Li_4Ti5O_{12}$ Nanosheet Anode. *Adv. Energy Mater.* **2017**, *7* (5), 1601825.

(24) Nazri, G.-A.; Pistoia, G. In *Lithium Batteries: Science and Technology*; Springer Science & Business Media: New York, 2008; pp 478−503.

(25) Qiu, H.; Yue, H.; Zhang, T.; Ju, Y.; Zhang, Y.; Guo, Z.; Wang, C.; Chen, G.; Wei, Y.; Zhang, D. Enhanced Electrochemical Performance of $Li_2FeSiO_4$/C Positive Electrodes for Lithium-Ion Batteries Via Yttrium Doping. *Electrochim. Acta* **2016**, *188*, 636−644.

(26) Kam, K. C.; Gustafsson, T.; Thomas, J. O. Synthesis and Electrochemical Properties of Nanostructured $Li_2FeSiO_4$/C Cathode Material for Li-Ion Batteries. *Solid State Ionics* **2011**, *192* (1), 356−359.

(27) Zhang, L.-L.; Duan, S.; Yang, X.-L.; Peng, G.; Liang, G.; Huang, Y.-H.; Jiang, Y.; Ni, S.-B.; Li, M. Reduced Graphene Oxide Modified $Li_2FeSiO_4$/C Composite with Enhanced Electrochemical Performance as Cathode Material for Lithium Ion Batteries. *ACS Appl. Mater. Interfaces* **2013**, *5* (23), 12304−12309.

(28) Yan, Z.; Cai, S.; Zhou, X.; Zhao, Y.; Miao, L. Sol-Gel Synthesis of Nanostructured $Li_2FeSiO_4$/C as Cathode Material for Lithium Ion Battery. *J. Electrochem. Soc.* **2012**, *159* (6), A894−A898.

(29) Shen, S.; Zhang, Y.; Wei, G.; Zhang, W.; Yan, X.; Xia, G.; Wu, A.; Ke, C.; Zhang, J. $Li_2FeSiO_4$/C Hollow Nanospheres as Cathode

Materials for Lithium-Ion Batteries. *Nano Res.* **2019**, *12* (2), 357−363.
(30) Xu, Y. M.; Shen, W.; Zhang, A. L.; Liu, H. M.; Ma, Z. F. Template-Free Hydrothermal Synthesis of $Li_2FeSiO_4$ Hollow Spheres as Cathode Materials for Lithium-Ion Batteries. *J. Mater. Chem. A* **2014**, *2* (32), 12982−12990.
(31) Fan, X.-Y.; Li, Y.; Wang, J.-J.; Gou, L.; Zhao, P.; Li, D.-L.; Huang, L.; Sun, S.-G. Synthesis and Electrochemical Performance of Porous $Li_2FeSiO_4$/C Cathode Material for Long-Life Lithium-Ion Batteries. *J. Alloys Compd.* **2010**, *493* (1−2), 77−80.
(32) Zhao, Y.; Li, J.; Wang, N.; Wu, C.; Ding, Y.; Guan, L. In Situ Generation of $Li_2FeSiO_4$ Coating on Mwnt as a High Rate Cathode Material for Lithium Ion Batteries. *J. Mater. Chem.* **2012**, *22* (36), 18797−18800.
(33) Zheng, J.; Myeong, S.; Cho, W.; Yan, P.; Xiao, J.; Wang, C.; Cho, J.; Zhang, J. G. Li-and Mn-Rich Cathode Materials: Challenges to Commercialization. *Adv. Energy Mater.* **2017**, *7* (6), 1601284.
(34) Jang, Y. I.; Huang, B.; Wang, H.; Sadoway, D. R.; Chiang, Y. M. Electrochemical Cycling-Induced Spinel Formation in High-Charge-Capacity Orthorhombic $LiMnO_2$. *J. Electrochem. Soc.* **1999**, *146* (9), 3217−3223.
(35) Yu, S.-H.; Yoon, T.; Mun, J.; Park, S.; Kang, Y.-S.; Park, J.-H.; Oh, S. M.; Sung, Y.-E. Continuous Activation of $Li_2mno_3$ Component Upon Cycling in $Li_{1.167}Ni_{0.233}Co_{0.100}Mn_{0.467}Mo_{0.033}O_2$ Cathode Material for Lithium Ion Batteries. *J. Mater. Chem. A* **2013**, *1* (8), 2833−2839.
(36) Ye, D.; Sun, C.; Chen, Y.; Ozawa, K.; Hulicova-Jurcakova, D.; Zou, J.; Wang, L. Ni-Induced Stepwise Capacity Increase in Ni-Poor Li-Rich Cathode Materials for High Performance Lithium Ion Batteries. *Nano Res.* **2015**, *8* (3), 808−820.
(37) Ye, D.; Zeng, G.; Nogita, K.; Ozawa, K.; Hankel, M.; Searles, D. J.; Wang, L. Understanding the Origin of $Li_2MnO_3$ Activation in Li-Rich Cathode Materials for Lithium-Ion Batteries. *Adv. Funct. Mater.* **2015**, *25* (48), 7488−7496.
(38) Ye, D.; Wang, B.; Chen, Y.; Han, G.; Zhang, Z.; Hulicova-Jurcakova, D.; Zou, J.; Wang, L. Understanding the Stepwise Capacity Increase of High Energy Low-Co Li-Rich Cathode Materials for Lithium Ion Batteries. *J. Mater. Chem. A* **2014**, *2* (44), 18767−18774.
(39) Rasool, M.; Chiu, H.-C.; Lu, X.; Voisard, F.; Gauvin, R.; Jiang, D.; Paolella, A.; Zaghib, K.; Demopoulos, G. P. Mechanochemically-Tuned Structural Annealing: A New Pathway to Enhancing Li-Ion Intercalation Activity in Nanosized $\beta_{II}$ $Li_2FeSiO_4$. *J. Mater. Chem. A* **2019**, *7*, 13705−13713.
(40) Yabuuchi, N.; Yamakawa, Y.; Yoshii, K.; Komaba, S. Low-Temperature Phase of $Li_2FeSiO_4$: Crystal Structure and a Preliminary Study of Electrochemical Behavior. *Dalton Trans.* **2011**, *40* (9), 1846−1848.
(41) Araujo, R. B.; Scheicher, R. H.; de Almeida, J.; da Silva, A. F.; Ahuja, R. First-Principles Investigation of Li Ion Diffusion in $Li_2FeSiO_4$. *Solid State Ionics* **2013**, *247*, 8−14.
(42) Liivat, A.; Thomas, J. O. Li-Ion Migration in $Li_2FeSiO_4$-Related Cathode Materials: A Dft Study. *Solid State Ionics* **2011**, *192* (1), 58−64.
(43) Araujo, R. B.; Scheicher, R. H.; De Almeida, J.; da Silva, A. F.; Ahuja, R. Lithium Transport Investigation in $Li_xFeSiO_4$: A Promising Cathode Material. *Solid State Commun.* **2013**, *173*, 9−13.
(44) Chen, Z. X.; Qiu, S.; Cao, Y. L.; Qian, J. F.; Ai, X. P.; Xie, K.; Hong, X. B.; Yang, H. X. Hierarchical Porous $Li_2FeSiO_4$/C Composite with 2 Li Storage Capacity and Long Cycle Stability for Advanced Li-Ion Batteries. *J. Mater. Chem. A* **2013**, *1* (16), 4988−4992.
(45) Lee, K. T.; Cho, J. Roles of Nanosize in Lithium Reactive Nanomaterials for Lithium Ion Batteries. *Nano Today* **2011**, *6* (1), 28−41.
(46) Vajeeston, P. Ionic Conductivity Enhancement by Particle Size Reduction in $Li_2FeSiO_4$. *Mater. Lett.* **2018**, *218*, 313−316.
(47) Armstrong, M. J.; O'Dwyer, C.; Macklin, W. J.; Holmes, J. D. Evaluating the Performance of Nanostructured Materials as Lithium-Ion Battery Electrodes. *Nano Res.* **2014**, *7* (1), 1−62.
(48) Wang, J.; Yang, J.; Tang, Y.; Liu, J.; Zhang, Y.; Liang, G.; Gauthier, M.; Karen Chen-Wiegart, Y.-c.; Norouzi Banis, M.; Li, X.; Li, R.; Wang, J.; Sham, T. K.; Sun, X. Size-Dependent Surface Phase Change of Lithium Iron Phosphate During Carbon Coating. *Nat. Commun.* **2014**, *5*, 1−8.
(49) Ferrari, A. C.; Robertson, J. Interpretation of Raman Spectra of Disordered and Amorphous Carbon. *Phys. Rev. B: Condens. Matter Mater. Phys.* **2000**, *61* (20), 14095−14107.
(50) Zeng, Y.; Chiu, H.-C.; Rasool, M.; Brodusch, N.; Gauvin, R.; Jiang, D.-T.; Ryan, D. H.; Zaghib, K.; Demopoulos, G. P. Hydrothermal Crystallization of $Pmn2_1$ $Li_2FeSiO_4$ Hollow Mesocrystals for Li-Ion Cathode Application. *Chem. Eng. J.* **2019**, *359*, 1592−1602.
(51) Armstrong, A. R.; Kuganathan, N.; Islam, M. S.; Bruce, P. G. Structure and Lithium Transport Pathways in $Li_2FeSiO_4$ Cathodes for Lithium Batteries. *J. Am. Chem. Soc.* **2011**, *133* (33), 13031−13035.
(52) Masese, T.; Tassel, C. d.; Orikasa, Y.; Koyama, Y.; Arai, H.; Hayashi, N.; Kim, J.; Mori, T.; Yamamoto, K.; Kobayashi, Y. Crystal Structural Changes and Charge Compensation Mechanism During Two Lithium Extraction/Insertion between $Li_2FeSiO_4$ and $FeSiO_4$. *J. Phys. Chem. C* **2015**, *119* (19), 10206−10211.
(53) Singh, S.; Panda, M. R.; Sen, R.; Johari, P.; Sinha, A.; Meena, S. S.; Mitra, S. Study of Higher Discharge Capacity, Phase Transition, and Relative Structural Stability in $Li_2FeSiO_4$ Cathode Upon Lithium Extraction Using an Experimental and Theoretical Approach and Full Cell Prototype Study. *ACS Appl. Energy Mater.* **2019**, *2* (9), 6584−6598.
(54) Billaud, J.; Eames, C.; Tapia-Ruiz, N.; Roberts, M. R.; Naylor, A. J.; Armstrong, A. R.; Islam, M. S.; Bruce, P. G. Evidence of Enhanced Ion Transport in Li-Rich Silicate Intercalation Materials. *Adv. Energy Mater.* **2017**, *7* (11), 1601043.
(55) Eames, C.; Armstrong, A. R.; Bruce, P. G.; Islam, M. S. Insights into Changes in Voltage and Structure of $Li_2FeSiO_4$ Polymorphs for Lithium-Ion Batteries. *Chem. Mater.* **2012**, *24* (11), 2155−2161.
(56) Sirisopanaporn, C.; Masquelier, C.; Bruce, P. G.; Armstrong, A. R.; Dominko, R. Dependence of $Li_2FeSiO_4$ Electrochemistry on Structure. *J. Am. Chem. Soc.* **2011**, *133* (5), 1263−1265.
(57) Seo, D.-H.; Kim, H.; Park, I.; Hong, J.; Kang, K. Polymorphism and Phase Transformations of $Li_{2-x}FeSiO_4$ ($0 \leqslant X \leqslant 2$) from First Principles. *Phys. Rev. B: Condens. Matter Mater. Phys.* **2011**, *84* (22), 220106.
(58) Levi, M.; Salitra, G.; Markovsky, B.; Teller, H.; Aurbach, D.; Heider, U.; Heider, L. Solid-State Electrochemical Kinetics of Li - Ion Intercalation into $Li_{1-X}CoO_2$: Simultaneous Application of Electroanalytical Techniques SSCV, PITT, and EIS. *J. Electrochem. Soc.* **1999**, *146* (4), 1279−1289.
(59) Fan, L.; Zhuang, H. L.; Gao, L.; Lu, Y.; Archer, L. A. Regulating Li Deposition at Artificial Solid Electrolyte Interphases. *J. Mater. Chem. A* **2017**, *5* (7), 3483−3492.
(60) Brodusch, N.; Demers, H.; Gauvin, R. The *f*-Ratio Method for X-Ray Microanalysis in the Sem. In *Field Emission Scanning Electron Microscopy*; Springer: Singapore, 2018; pp 55−65.
(61) Dippel, C.; Krueger, S.; Kraft, V.; Nowak, S.; Winter, M.; Li, J. Aging Stability of $Li_2FeSiO_4$ Polymorphs in $LiPF_6$ Containing Organic Electrolyte for Lithium-Ion Batteries. *Electrochim. Acta* **2013**, *105*, 542−546.
(62) Dippel, C.; Krueger, S.; Kloepsch, R.; Niehoff, P.; Hoffmann, B.; Nowak, S.; Passerini, S.; Winter, M.; Li, J. Aging of $Li_2FeSiO_4$ Cathode Material in Fluorine Containing Organic Electrolytes for Lithium-Ion Batteries. *Electrochim. Acta* **2012**, *85*, 66−71.
(63) Ensling, D.; Stjerndahl, M.; Nytén, A.; Gustafsson, T.; Thomas, J. O. A Comparative Xps Surface Study of $Li_2FeSiO_4$/C Cycled with LiTFSi-and $LiPF_6$-Based Electrolytes. *J. Mater. Chem.* **2009**, *19* (1), 82−88.
(64) Choudhury, S.; Archer, L. A. Lithium Fluoride Additives for Stable Cycling of Lithium Batteries at High Current Densities. *Adv. Electron. Mater.* **2016**, *2* (2), 1500246.
(65) Chiu, H.-C.; Lu, X.; Zhou, J.; Gu, L.; Reid, J.; Gauvin, R.; Zaghib, K.; Demopoulos, G. P. Annealing-Regulated Elimination of


https://dx.doi.org/10.1021/acs.jpcc.9b11896
J. Phys. Chem. C 2020, 124, 5966−5977

Residual Strain-Induced Structural Relaxation for Stable High-Power $Li_4Ti5O_{12}$ Nanosheet Anodes. *Nano Energy* **2017**, *32*, 533−541.
(66) Laffont, L.; Delacourt, C.; Gibot, P.; Wu, M. Y.; Kooyman, P.; Masquelier, C.; Tarascon, J. M. Study of the $LiFePO_4/FePO_4$ Two-Phase System by High-Resolution Electron Energy Loss Spectroscopy. *Chem. Mater.* **2006**, *18* (23), 5520−5529.
(67) Castro, F. C.; Dravid, V. P. Characterization of Lithium Ion Battery Materials with Valence Electron Energy-Loss Spectroscopy. *Microsc. Microanal.* **2018**, *24* (3), 214−220.



https://dx.doi.org/10.1021/acs.jpcc.9b11896
*J. Phys. Chem. C* 2020, 124, 5966−5977